Research Article | Vol. 8, No. 10 | 1 Oct 2017 | BIOMEDICAL OPTICS EXPRESS 4687
Biomedical Optics EXPRESS

Efficient quantitative phase microscopy using programmable annular LED illumination

JIAJI LI,[1,2,3,4] QIAN CHEN,[1,2] JIALIN ZHANG,[1,2,3] YAN ZHANG,[1,2,3] LINPENG LU,[1,2,3] AND CHAO ZUO[1,2,3,*]

[1] *School of Electronic and Optical Engineering, Nanjing University of Science and Technology, No. 200 Xiaolingwei Street, Nanjing, Jiangsu Province 210094, China*
[2] *Jiangsu Key Laboratory of Spectral Imaging & Intelligent Sense, Nanjing University of Science and Technology, Nanjing, Jiangsu Province 210094, China*
[3] *Smart Computational Imaging (SCI) Laboratory, Nanjing University of Science and Technology, Nanjing, Jiangsu Province 210094, China*
[4] *jiajili@njust.edu.cn*
[*] *zuochao@njust.edu.cn*

Abstract: In this work, we present an efficient quantitative phase imaging (QPI) approach using programmable annular LED illumination. As a new type of coded light source, the LED array provides flexible illumination control for noninterferometric QPI based on a traditional microscopic configurations. The proposed method modulates the transfer function of system by changing the LED illumination pattern, which provides noise-robust response of transfer function and achieves twice resolution limit of objective NA. The quantitative phase can be recovered from slightly defocused intensity images through inversion of transfer function. Moreover, the weak object transfer function (WOTF) of axis-symmetric oblique source is derived, and the noise-free and noisy simulation results validate the predicted theory. Finally, we experimentally confirm accurate and repeatable performance of our method by imaging calibrated phase samples and cellular specimens with different NA objectives.

OCIS codes: (100.5070) Phase retrieval; (180.0180) Microscopy; (100.3010) Image reconstruction techniques; (170.3880) Medical and biological imaging.

References and links

1. E. Barone-Nugent, A. Barty, and K. Nugent, "Quantitative phase-amplitude microscopy I: optical microscopy," J. Microsc. **206**, 194–203 (2002).
2. G. Popescu, T. Ikeda, R. R. Dasari, and M. S. Feld, "Diffraction phase microscopy for quantifying cell structure and dynamics," Opt. Lett. **31**, 775–777 (2006).
3. D. Paganin, T. Gureyev, S. Mayo, A. Stevenson, Y. I. Nesterets, and S. Wilkins, "X-ray omni microscopy," J. Microsc. **214**, 315–327 (2004).
4. S. Bajt, A. Barty, K. Nugent, M. McCartney, M. Wall, and D. Paganin, "Quantitative phase-sensitive imaging in a transmission electron microscope," Ultramicroscopy **83**, 67–73 (2000).
5. G. Popescu, Y. Park, N. Lue, C. Best-Popescu, L. Deflores, R. R. Dasari, M. S. Feld, and K. Badizadegan, "Optical imaging of cell mass and growth dynamics," Am. J. Physiol. **295**, C538–C544 (2008).
6. Y. Park, C. A. Best, K. Badizadegan, R. R. Dasari, M. S. Feld, T. Kuriabova, M. L. Henle, A. J. Levine, and G. Popescu, "Measurement of red blood cell mechanics during morphological changes," Proc. Natl. Acad. Sci. **107**, 6731–6736 (2010).
7. F. Zernike, "Phase contrast, a new method for the microscopic observation of transparent objects," Physica **9**(7), 686–698 (1942).
8. G. Nomarski and A. Weill, "Application à la métallographie des méthodes interférentielles à deux ondes polarisées," Rev. Metall **2**, 121–128 (1955).
9. M. K. Kim, *Digital Holographic Microscopy* (Springer, New York 2011).
10. P. Ferraro, D. Alferi, S. De Nicola, L. De Petrocellis, A. Finizio, and G. Pierattini, "Quantitative phase-contrast microscopy by a lateral shear approach to digital holographic image reconstruction," Opt. Lett. **31**, 1405–1407 (2006).
11. A. Ahmad, V. Dubey, G. Singh, V. Singh, and D. S. Mehta, "Quantitative phase imaging of biological cells using spatially low and temporally high coherent light source," Opt. Lett. **41**, 1554–1557 (2016).
12. J. Dohet-Eraly, C. Yourassowsky, A. El Mallahi, and F. Dubois, "Quantitative assessment of noise reduction with partial spatial coherence illumination in digital holographic microscopy," Opt. Lett. **41**, 111–114 (2016).

#300860 https://doi.org/10.1364/BOE.8.004687
Journal © 2017 Received 28 Jun 2017; revised 12 Sep 2017; accepted 19 Sep 2017; published 26 Sep 2017

Biomedical Optics EXPRESS

13. Z. Wang, L. Millet, M. Mir, H. Ding, S. Unarunotai, J. Rogers, M. U. Gillette, and G. Popescu, "Spatial light interference microscopy (SLIM)," Opt. Express **19**, 1016–1026 (2011).
14. Basanta Bhaduri, Hoa Pham, Mustafa Mir, and Gabriel Popescu, "Diffraction phase microscopy with white light," Opt. Lett. **37**, 1094–1096 (2012).
15. M. R. Teague, "Deterministic phase retrieval: a Greens function solution," J. Opt. Soc. Am. **73**(11), 1434–1441 (1983).
16. N. Streibl, "Phase imaging by the transport equation of intensity," Opt. Commun. **49**, 6–10 (1984).
17. A. Barty, K. A. Nugent, D. Paganin, and A. Roberts, "Quantitative optical phase microscopy," Opt. Lett. **23**, 817–819 (1998).
18. C. Zuo, Q. Chen, W. Qu, and A. Asundi, "Noninterferometric single-shot quantitative phase microscopy," Opt. Lett. **38**, 3538–3541 (2013).
19. M. H. Jenkins and T. K. Gaylord, "Quantitative phase microscopy via optimized inversion of the phase optical transfer function," Appl. Opt. **54**, 8566–8579 (2015).
20. J. Li, Q. Chen, J. Sun, J. Zhang, and C. Zuo, "Multimodal computational microscopy based on transport of intensity equation," J. Biomed. Opt. **21**, 126003 (2016).
21. T. E. Gureyev, A. Roberts, and K. A. Nugent, "Partially coherent fields, the transport-of-intensity equation, and phase uniqueness," J. Opt. Soc. Am. A **12**, 1942–1946 (1995).
22. D. Paganin and K. A. Nugent, "Noninterferometric phase imaging with partially coherent light," Phys. Rev. Lett. **80**, 2586 (1998).
23. J. C. Petruccelli, L. Tian, and G. Barbastathis, "The transport of intensity equation for optical path length recovery using partially coherent illumination," Opt. Express **21**, 14430–14441 (2013).
24. M. H. Jenkins, J. M. Long, and T. K. Gaylord, "Multifilter phase imaging with partially coherent light," Appl. Opt. **53**, D29–D39 (2014).
25. J. W. Goodman, *Introduction to Fourier Optics* (Roberts and Company Publishers, 2005).
26. T. H. Nguyen, C. Edwards, L. L. Goddard, and G. Popescu, "Quantitative phase imaging of weakly scattering objects using partially coherent illumination," Opt. Express **24**, 11683–11693 (2016).
27. N. Streibl, "Three-dimensional imaging by a microscope," J. Opt. Soc. Am. A **2**, 121–127 (1985).
28. C. J. Sheppard, "Defocused transfer function for a partially coherent microscope and application to phase retrieval," J. Opt. Soc. Am. A **21**, 828–831 (2004).
29. S. S. Kou, L. Waller, G. Barbastathis, P. Marquet, C. Depeursinge, and C. J. Sheppard, "Quantitative phase restoration by direct inversion using the optical transfer function," Opt. Lett. **36**, 2671–2673 (2011).
30. C. Zuo, Q. Chen, Y. Yu, and A. Asundi, "Transport-of-intensity phase imaging using Savitzky-Golay differentiation filter-theory and applications," Opt. Express **21**, 5346–5362 (2013).
31. A. Pogany, D. Gao, and S. Wilkins, "Contrast and resolution in imaging with a microfocus x-ray source," Rev. Sci. Instrum. **68**, 2774–2782 (1997).
32. J. P. Guigay, M. Langer, R. Boistel, and P. Cloetens, "Mixed transfer function and transport of intensity approach for phase retrieval in the Fresnel region," Opt. Lett. **32**, 1617–1619 (2007).
33. A. M. Zysk, R. W. Schoonover, P. S. Carney, and M. A. Anastasio, "Transport of intensity and spectrum for partially coherent fields," Opt. Lett. **35**, 2239–2241 (2010).
34. C. Zuo, Q. Chen, L. Tian, L. Waller, and A. Asundi, "Transport of intensity phase retrieval and computational imaging for partially coherent fields: The phase space perspective," Opt. Laser Eng. **71**, 20–32 (2015).
35. C. J. Sheppard, "Three-dimensional phase imaging with the intensity transport equation," Appl. Opt. **41**, 5951–5955 (2002).
36. C. Zuo, J. Sun, J. Li, J. Zhang, A. Asundi, and Q. Chen, "High-resolution transport-of-intensity quantitative phase microscopy with annular illumination," Sci. Rep. **7**, 7654 (2017).
37. G. Zheng, R. Horstmeyer, and C. Yang, "Wide-field, high-resolution Fourier ptychographic microscopy," Nat. Photonics **7**, 739–745 (2013).
38. J. Sun, C. Zuo, L. Zhang, and Q. Chen, "Resolution-enhanced Fourier ptychographic microscopy based on high-numerical-aperture illuminations," Sci. Rep. **7**, 1187 (2017).
39. L. Tian and L. Waller, "Quantitative differential phase contrast imaging in an LED array microscope," Opt. Express **23**, 11394–11403 (2015).
40. C. Zuo, J. Sun, J. Zhang, Y. Hu, and Q. Chen, "Lensless phase microscopy and diffraction tomography with multi-angle and multi-wavelength illuminations using a LED matrix," Opt. Express **23**, 14314–14328 (2015).
41. J. Li, Q. Chen, J. Zhang, Z. Zhang, Y. Zhang, and C. Zuo, "Optical diffraction tomography microscopy with transport of intensity equation using a light-emitting diode array," Opt. Laser Eng. **95**, 26–34 (2017).
42. E. Wolf, "Three-dimensional structure determination of semi-transparent objects from holographic data," Opt. Commun. **1**, 153–156 (1969).
43. K. Kim, J. Yoon, S. Shin, S. Lee, S.-A. Yang, and Y. Park, "Optical diffraction tomography techniques for the study of cell pathophysiology," J. Biomed. Photon. Eng. **2** (2016).
44. S. B. Mehta and C. J. Sheppard, "Quantitative phase-gradient imaging at high resolution with asymmetric illumination-based differential phase contrast," Opt. Lett. **34**, 1924–1926 (2009).
45. A. B. Parthasarathy, K. K. Chu, T. N. Ford, and J. Mertz, "Quantitative phase imaging using a partitioned detection aperture," Opt. Lett. **37**, 4062–4064 (2012).

Biomedical Optics EXPRESS

46. C. Zuo, J. Sun, S. Feng, M. Zhang, and Q. Chen, "Programmable aperture microscopy: A computational method for multi-modal phase contrast and light field imaging," Opt. Laser Eng. **80**, 24–31 (2016).
47. J. M. Cowley, *Diffraction Physics* (Elsevier, 1995).
48. H. Hopkins, "On the diffraction theory of optical images," Proc. Phys. Soc. London A **217**, 408–432 (1953).
49. M. Born and E. Wolf, Principles of Optics, 7th edition, (Pergamon, 1999), chap. **9**.

1. Introduction

Phase imaging plays a crucial role in the fields of optical, X-ray and electron microscopy [1–4]. The phase of biological cells and tissues carries important information about the structure and intrinsic optical properties in microscopic imaging [5, 6]. Although this information can not be directly recorded by the digital detector (CCD or CMOS), the Zernike phase contrast microscopy [7] and differential interference contrast (DIC) microscopy [8] can provide reliable phase contrast about the transparent cells and weakly absorbing objects via converting the phase into intensity. However, these techniques are only used for the visualized and qualitative imaging instead of giving quantitative maps of phase change, which make the quantitative data interpretation and phase reconstruction difficult.

Quantitative phase imaging (QPI) is a powerful tool for wide-ranging biomedical research and characterization of optical elements, which can realize the quantitative reconstruction of the sample information due to its label-free and unique capabilities to image the phase or the optical path thickness of cells, tissues, and optical fibers. As a conventional interferometric approach of QPI, off-axis digital holographic microscopy (DHM) [9, 10] measures the phase delay quantitatively introduced by the heterogeneous refractive index distribution within the specimen. Such method requires a coherent illumination source and a relatively vibration-sensitive optical system, and the speckle noise of laser degrades the spatial resolution of phase image [11, 12]. Other white-light QPI approaches based on common path geometries have been developed to alleviate the problem of coherent noise and enhance the stability of mechanical vibrations [13, 14], thus the spatial resolution and imaging quality of phase measurement are greatly improved. Nevertheless, all above-mentioned methods still rely on spatially coherent illumination, and the maximum achievable resolution of phase imaging is restricted to the coherent diffraction limit.

On the other hand, the deterministic phase retrieval can be also realized by the transport of intensity equation (TIE) [15–17] only using object field intensities at multiple axially displaced planes. The TIE linearizes the relationship between the phase and derivative of intensity along the axis of propagation [15], then the direct phase can be uniquely determined by solving the TIE with intensity images and the longitudinal intensity derivative on the in-focus plane. QPI based on TIE has been increasingly investigated in micro-optics inspection and dynamic phase imaging of biological processes in recent years due to its unique advantages over interferometric techniques to achieve quantitative reconstruction result without the need for complicated interferometric optical configurations, reference beam, laser illumination sources and phase unwrapping [18–20]. It has been demonstrated that the noninterferometric phase retrieval methods based on TIE can be well adapted to partially coherent illumination [21–24] in spite of the fact that the original derivation of TIE is established on the paraxial approximation and coherent illumination. Due to the nonlinear relationship among the intensity image of object, partially coherent source, and optical system, the imaging process and mathematical modeling become more complicated than coherent situation [25, 26]. Nevertheless, the phase retrieval of TIE can be reformulated informatively using the concept of weak object transfer function (WOTF) under weak defocusing assumptions, and the self-interference of scattered light, called bilinear terms, can be ignored [27–30]. The WOTF describes the frequency domain response of phase and absorption for an optical imaging system, which has been also called the contrast transfer function (CTF) in the field of propagation-based X-ray phase imaging [31, 32].

Although the reconstructed phase from TIE is not well-defined over the partially coherent field,

Biomedical Optics EXPRESS

the definition of "phase" has been proven to be the weighted average superposition of phase under various coherent illumination using the theory of coherent mode decomposition [33], and this definition can be converted to the well-defined optical path length of sample [23]. The physical meaning of phase for partially coherent field is related to the transverse Poynting vector [21] or Wigner distribution moment [34]. Under coherent illumination, the transfer function would be limited by the objective NA, and the poor response of TIE at low spatial frequency amplifies the noise and leads to the cloud-like artifacts superimposed on the reconstructed phase [17,18]. While in the case of partially coherent illumination, the maximum achievable resolution of phase imaging is extended to the sum of objective NA and illumination NA over coherent situation, where the ratio of illumination NA to objective NA is called coherence parameter $s = NA_{ill}/NA_{obj}$. As the value of parameter s becomes larger ($NA_{ill} \leq NA_{obj}$ actually), the phase contrast of defocused intensity image is vanished dramatically due to the attenuated response of transfer function. While the illumination NA approaches objective NA, the spatial cutoff frequency is increased to twice the objective NA as predicted by the WOTF [27–29,35]. But meanwhile, the low contrast intensity images would lead to the disadvantage that the signal-to-noise ratio (SNR) is too bad to recover the phase from the defocused intensity images. The imaginary part of WOTF of large defocus distance rises faster than small defocus distance at low frequency near zero, so most of phase retrieval methods based on multiple defocus planes select the low frequency components of large defocus WOTF as the optimal one [20,24,30]. However, the transfer function of phase under large defocus distance contains too many zero crossings due to the rhythmical fluctuation of sine function, and these points make it almost impossible to recover the phase information of high frequency.

In this paper, we present an efficient QPI approach which combines the annular aperture and programmable LED illumination by replacing traditional halogen illumination source with a LED array within a conventional transmission microscope. The annular illumination pattern matched with objective pupil is displayed on the LED array and each isolated LED is treated as a coherent source. The WOTF of axis-symmetric oblique source in arbitrary position on source pupil plane is derived, and the principle of discrete annular LED illumination pattern is validated as well. Not only the spatial resolution of final reconstructed phase can be extended to twice the objective NA, but also the phase contrast of defocused intensity image is strong because the response of phase transfer function (PTF) with annular source tends to be roughly constant across a wide range of frequencies, which is an ideal form for noise-robust, high-resolution, and well-posed phase reconstruction. Even though this TIE-based QPI approach utilizing annular illumination has been reported by our group in an earlier paper [36], and the LED array has also been employed for Fourier ptychography [37,38] and other QPI modalities [39–41], the present work further derive the WOTF for axis-symmetric oblique source, and develop this discrete source to the superposition of arbitrary illumination pattern, such as circular illumination, annular illumination, or any other axis-symmetric illumination. Furthermore, the combination of annular illumination and programmable LED array makes the modulation of illumination more flexible and compatible without the need for real annular apertures which conventionally rely on intricate alterations and realignment when changing the objectives [36]. These advantages make it into a competitive and powerful alternative to traditional bright-field illumination approaches for wide variety of biomedical investigations, micro-optics inspection and biophotonics. The noise-free and noisy simulation results validate the applicability of discrete annular source sufficiently, and the quantitative phase measurements of a micro polystyrene bead and visible blazed transmission grating demonstrate the accuracy of this method. The experimental investigations of unstained human cancer cells using different types objective are presented, and this results show the possibility of widespread adoption of QPI in the morphology study of cellular processes and biomedical community.

Biomedical Optics EXPRESS

2. Principle

2.1. WOTF for axis-symmetric oblique source

In the standard $6f$ optical configuration, as illustrated in Fig. 1 in [27], an object is illuminated by a Köhler illumination source and imaged via an objective lens. The image formation of this telecentric microscopic imaging system can be described by Fourier transforms and a linear filtering operation in the pupil plane [25]. For the incoherent case, the intensity image can be given by the convolution equation $I(\mathbf{r}) = |h(\mathbf{r})|^2 \otimes |t(\mathbf{r})|^2 = |h(\mathbf{r})|^2 \otimes I_u(\mathbf{r})$, where h denotes the amplitude point spread function (PSF) of the imaging system, t is the complex amplitude, and I_u represents the intensities of coherent partial images arising from all light source points. On a different note, in the coherent case it obeys $I(\mathbf{r}) = |h(\mathbf{r}) \otimes t(\mathbf{r})|^2$. Thus, the incoherent system is linear in intensity, whereas the coherent system is nonlinear in that quantity [25]. More information about how to obtain the intensity under partially coherent illumination can be found in the Appendix A.

Due to the fact that above image formation is neither linear in amplitude nor linear in intensity, the mathematical derivation of phase recovery becomes more complicated for partially coherent system [25, 26]. To simplify this theoretical modeling, one way is to assume that the observed sample is a weak phase object, and the first-order Taylor expansion of complex amplitude can be described as:

$$t(\mathbf{r}) \equiv a(\mathbf{r}) \exp[i\phi(\mathbf{r})] \approx a(\mathbf{r}) [1 + i\phi(\mathbf{r})]^{a(\mathbf{r})=a_0+\Delta a(\mathbf{r})} \approx a_0 + \Delta a(\mathbf{r}) + i a_0 \phi(\mathbf{r}) \tag{1}$$

where $a(\mathbf{r})$ is the amplitude with a mean value of a_0, and $\phi(\mathbf{r})$ is the phase distribution. Implementing Fourier transform on t and multiplying it with its conjugate form, the bilinear terms can be neglected because the scattered light is weak compared to the unscattered light for a weak phase object. The formula of complex conjugate multiplication can be approximated as:

$$\begin{aligned} T(\mathbf{u}_1) T^*(\mathbf{u}_2) =& a_0^2 \delta(\mathbf{u}_1) \delta(\mathbf{u}_2) + a_0 \delta(\mathbf{u}_2) \left[\Delta\widetilde{a}(\mathbf{u}_1) + i a_0 \widetilde{\phi}(\mathbf{u}_1)\right] \\ &+ a_0 \delta(\mathbf{u}_1) \left[\Delta\widetilde{a}^*(\mathbf{u}_2) - i a_0 \widetilde{\phi}^*(\mathbf{u}_2)\right]. \end{aligned} \tag{2}$$

The approximation used in Eq. (2) corresponds to the first-order Born approximation, and this approximation is commonly used in optical diffraction tomography [42, 43]. While the two cross-related points coincide with each other in frequency domain, the intensity image of weak object under the partially coherent field can be rewritten as the following equation by substitute Eq. (2) into Eq. (27) in the Appendix A:

$$I(\mathbf{r}) = a_0^2 TCC(0;0) + 2a_0 \mathrm{Re}\left\{\int TCC(\mathbf{u};0) \left[\Delta\widetilde{a}(\mathbf{u}) + i a_0 \widetilde{\phi}(\mathbf{u})\right] \exp(i2\pi \mathbf{r}\mathbf{u})\, d\mathbf{u}\right\} \tag{3}$$

where the $TCC(\mathbf{u};0)$ is equal to $TCC^*(0;\mathbf{u})$ due to the conjugate symmetry of transmission cross coefficient (TCC). The intensity contributions of various system components (eg. source and object) are separated and decoupled in Eq. (3), and the $TCC(\mathbf{u};0)$ can be expressed as WOTF:

$$WOTF(\mathbf{u}) \equiv TCC(\mathbf{u};0) = \iint S\left(\mathbf{u}'\right) P^*\left(\mathbf{u}'\right) P\left(\mathbf{u}' + \mathbf{u}\right) d\mathbf{u}' \tag{4}$$

where $\mathbf{u}'$ represents the variable in Fourier polar coordinate. The WOTF is real and even as long as the distribution of source $S(\mathbf{u})$ or objective pupil $P(\mathbf{u})$ is axis-symmetric, thus the intensity image on the in-focus plane gives no phase contrast but absorption contrast. Some other asymmetric methods can produce the phase contrast in the in-focus intensity image by breaking the symmetry of $S(\mathbf{u})$ or $P(\mathbf{u})$. The prominent examples are differential phase contrast microscopy [39, 44] and partitioned or programmable aperture microscopy [45, 46]. The defocusing of optical system

Biomedical Optics EXPRESS

along the z axis, which is another more convenient way to produce phase contrast and imaginary part, would be introduced into the pupil function:

$$P(\mathbf{u}) = |P(\mathbf{u})|\, e^{ikz\sqrt{1-\lambda^2|\mathbf{u}|^2}},\ \lambda|\mathbf{u}| \le 1 \tag{5}$$

where z is the defocus distance along the optical axis. Substituting the complex pupil function into Eq. (4) yields a complex WOTF:

$$WOTF(\mathbf{u}) = \iint S\left(\mathbf{u}'\right)\left|P^*\left(\mathbf{u}'\right)\right|\left|P\left(\mathbf{u}'+\mathbf{u}\right)\right| \exp\left[ikz\left(-\sqrt{1-\lambda^2|\mathbf{u}'|^2}+\sqrt{1-\lambda^2|\mathbf{u}+\mathbf{u}'|^2}\right)\right] d\mathbf{u}' \tag{6}$$

The components of amplitude transfer function (ATF) and PTF correspond to the real and imaginary parts of WOTF, respectively:

$$\begin{aligned} H_A(\mathbf{u}) &= 2a_0\,\mathrm{Re}\left[WOTF(\mathbf{u})\right] \\ H_P(\mathbf{u}) &= 2a_0\,\mathrm{Im}\left[WOTF(\mathbf{u})\right]. \end{aligned} \tag{7}$$

Considering that the upright incident coherent source is a special case of oblique illumination, the derivation of WOTF for oblique source will be processed under the same framework for these two different types illumination. There is a pair of ideal axis-symmetric light spots on the source pupil plane, and the distance from these points to the center of pupil is $\boldsymbol{\rho}_s$ (spatially normalized frequency). The intensity distribution of this source pupil can be expressed as:

$$S(\mathbf{u}) = \delta(\mathbf{u}-\boldsymbol{\rho}_s) + \delta(\mathbf{u}+\boldsymbol{\rho}_s) \tag{8}$$

Substituting this pupil function into Eq. (6) results in a complex (but even) WOTF for oblique situation

$$\begin{aligned} WOTF_{obl}(\mathbf{u}) = &|P(\mathbf{u}-\boldsymbol{\rho}_s)|\, e^{ikz\left(-\sqrt{1-\lambda^2|\boldsymbol{\rho}_s|^2}+\sqrt{1-\lambda^2|\mathbf{u}-\boldsymbol{\rho}_s|^2}\right)} \\ &+ |P(\mathbf{u}+\boldsymbol{\rho}_s)|\, e^{ikz\left(-\sqrt{1-\lambda^2|\boldsymbol{\rho}_s|^2}+\sqrt{1-\lambda^2|\mathbf{u}+\boldsymbol{\rho}_s|^2}\right)} \end{aligned} \tag{9}$$

where $|P(\mathbf{u}-\boldsymbol{\rho}_s)|$ and $|P(\mathbf{u}+\boldsymbol{\rho}_s)|$ are the pair of aperture functions shifted by the oblique coherent source in Fourier space. The aperture function for a circular objective pupil with normalized radius $\boldsymbol{\rho}_p$ is given by

$$|P(\mathbf{u})| = \begin{cases} 1, & \text{if } \mathbf{u} \le \boldsymbol{\rho}_p \\ 0, & \text{if } \mathbf{u} > \boldsymbol{\rho}_p. \end{cases} \tag{10}$$

For the coherent case ($\boldsymbol{\rho}_s$=0), the WOTF can be greatly simplified as:

$$WOTF_{coh}(\mathbf{u}) = |P(\mathbf{u})|\, e^{ikz\left(-1+\sqrt{1-\lambda^2|\mathbf{u}|^2}\right)}. \tag{11}$$

Two aperture functions are overlapped with each other in this coherent situation, so the values of final coherent WOTF is only half. The absorption and phase contrast are given by the real and imaginary parts of $WOTF_{coh}$ using Euler's formula as shown in Eq. (7). By further invoking the paraxial approximation and replacing $\sqrt{1-\lambda^2\mathbf{u}^2}$ with $1-\lambda^2\mathbf{u}^2/2$, the imaginary part of the $WOTF_{coh}$ can be written as a sine term $\sin\left(\pi\lambda z|\mathbf{u}|^2\right)$. Under the conditions of weak defocusing, this transfer function can be further approximated by a parabolic function

$$H_p(\mathbf{u})_{TIE} = |P(\mathbf{u})| \sin\left(\pi\lambda z|\mathbf{u}|^2\right) \approx |P(\mathbf{u})|\,\pi\lambda z|\mathbf{u}|^2 \tag{12}$$

This Laplacian operator is corresponding to the PTF of TIE in Fourier domain, and the two-dimensional (2D) image of WOTF for coherent source under weak defocusing conditions is

Biomedical Optics EXPRESS

shown in Fig. 1(a1). The line profiles of TIE and PTF for various defocus distances are illustrated in Fig. 1(a2) as well. It is obvious that the profile of TIE is consistent with the PTF for weak defocus distance (0.5 μm) at low frequency. Therefore, the coherent transfer function is getting closer to the TIE as long as the defocus distance is getting smaller. In other words, the TIE is a special case of coherent transfer function under weak defocusing.

On the other hand, these two coherent points do not coincide with each other in the center of the source plane, as shown in Fig. 1(b1) and 1(c1). The imaginary part of Eq. (9) is limited by their own pupil functions, thus the PTF for oblique point source can be written as:

$$\begin{aligned} H_p(\mathbf{u})_{obl} = & \frac{1}{2}\left|P\left(\mathbf{u}-\boldsymbol{\rho}_s\right)\right| \sin\left[kz\left(\sqrt{1-\lambda^2|\mathbf{u}-\boldsymbol{\rho}_s|^2}-\sqrt{1-\lambda^2|\boldsymbol{\rho}_s|^2}\right)\right] \\ & + \frac{1}{2}\left|P\left(\mathbf{u}+\boldsymbol{\rho}_s\right)\right| \sin\left[kz\left(\sqrt{1-\lambda^2|\mathbf{u}+\boldsymbol{\rho}_s|^2}-\sqrt{1-\lambda^2|\boldsymbol{\rho}_s|^2}\right)\right] \end{aligned} \tag{13}$$

Figure 1(b2) and 1(c2) show the curves of PTF for different $\boldsymbol{\rho}_s$ and defocus distances, respectively.

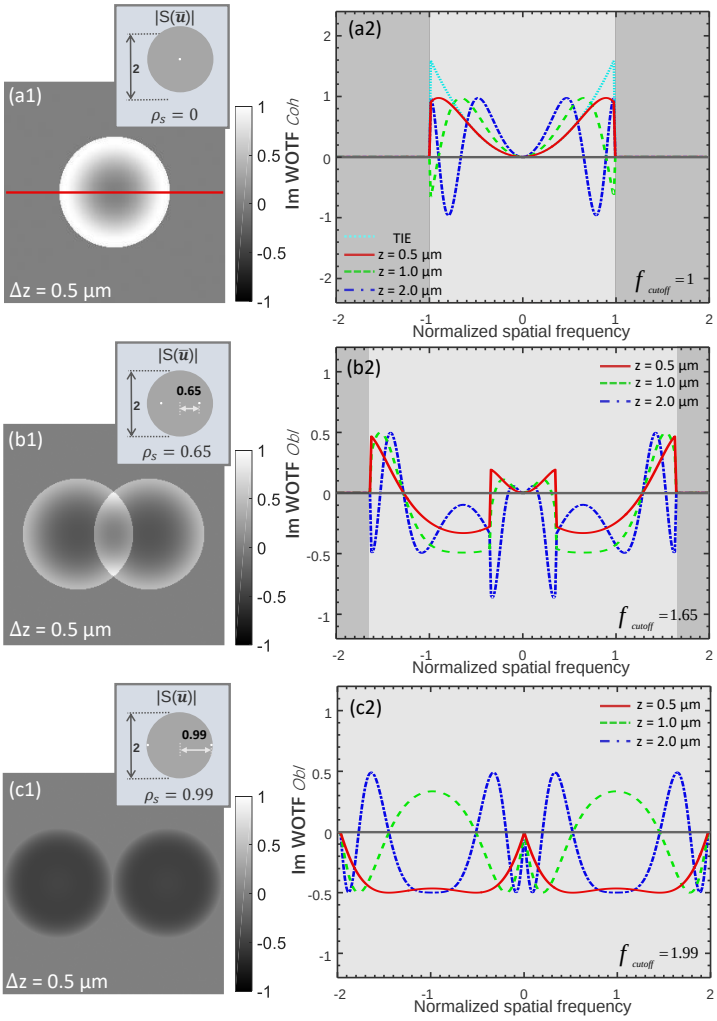

Fig. 1. 2D images of PTF for different types axis-symmetric source under weak defocusing conditions and the line profiles of TIE and PTF for various defocus distances.

Biomedical Optics EXPRESS

The cutoff frequency of transfer function is determined by the shifted aperture functions, and the achievable imaging resolution, which is equal to $\boldsymbol{\rho}_p+\boldsymbol{\rho}_s$, is getting larger with the increase of $\boldsymbol{\rho}_s$ in the oblique direction. Nevertheless, the line profiles of these transfer functions has two jump edges due to the superposition of two shifted objective pupil functions in Fig. 1(b2). The jump edge would induce zero crossings and make the response of frequency bad around these points, and such edges should be avoided as much as possible. While this pair of source points matches objective pupil ($\boldsymbol{\rho}_p \approx \boldsymbol{\rho}_s$), not only the cutoff frequency of PTF can be extended to twice the resolution of coherent diffraction limit, but also the response of PTF is roughly constant in a specific direction under this axis-symmetric oblique illumination.

2.2. Validation of discrete annular LED illumination

For any axis-symmetric shape of partially coherent illumination, a certain illumination pattern can be discretized into a lot of coherent point sources with finite-size including oblique and upright incident light points. The image formation of an optical microscopic system under partially coherent field can be simply understood as a convolution with a magnified replica of each discrete coherent source. Moreover, for the optical imaging with Köhler illumination, this process is coincident with the incoherent superposition of all intensities of the coherent partial images arising from all discrete light source points [25, 33]. While the condenser aperture iris diaphragm becomes bigger, the maximum achievable imaging resolution of intensity image is also getting bigger and the depth of field (DOF) becomes shallower as we knew it. However, the phase contrast (as well as absorption contrast) of the defocused image will become weaker, and the contrast attenuation of captured intensity image will reduce the SNR of phase reconstruction while the coherence parameter s continues to grow [27, 36]. So the recommended range of parameter s is from 0.7 to 0.8 for proper image resolution and contrast in most microscope instruction manual.

To overcome the tradeoff between image contrast and resolution, programmable annular illumination is adopted which is different from the traditional circular diaphragm aperture for QPI microscopy. The LED array is placed in the front focal plane of condenser to illuminate the specimen, and each single LED can be controlled separately. A test image, which is used to simulate the discrete LED array, with 512×512 pixels whose size is 0.176 μm and an objective with 0.75 NA are employed for the validation of annular LED illumination. While a pair of oblique illumination points is located on the edge of source pupil, it can be known that the imaging resolution is twice the NA of the objective in oblique direction as shown in Fig. 1(c). Thus, three different types of discrete annular patterns and one circular pattern are utilized for the comparison of WOTF under same system parameter. The expression of annular source can be written as the sum of delta function

$$S(\mathbf{u}) = \sum_{i=0}^{N} \delta(\mathbf{u} - \mathbf{u_i}), \quad |\mathbf{u}_i| \approx \left|\boldsymbol{\rho}_p\right| \tag{14}$$

where N is the number of all discrete light points on the source plane.

Figure 2 shows the 2D images and line profiles of WOTF imaginary part for various annular illumination patterns and defocus distances. There are four LEDs on the top-bottom and left-right of source plane in Fig. 2(a), thus the double imaging resolution of objective NA can be obtained in the vertical and horizontal directions. While eight LEDs can cover twice the cutoff frequency of objective in four different directions, and the PTF image of eight LEDs seems to be the superposition of transfer function for several pairs of axis-symmetric oblique sources. For the continuous situation of annular illumination, as shown in Fig. 2(c), the final PTF provides isotropic imaging resolution in all directions. In addition to above three different types of annular shape, the PTF of circular illumination aperture is illustrated in Fig. 2(d) and the cutoff frequency is extended to twice the NA of the objective as well. However, the response of transfer function of circular aperture is diminished dramatically compared to above three annular shapes. It is

Biomedical Optics EXPRESS

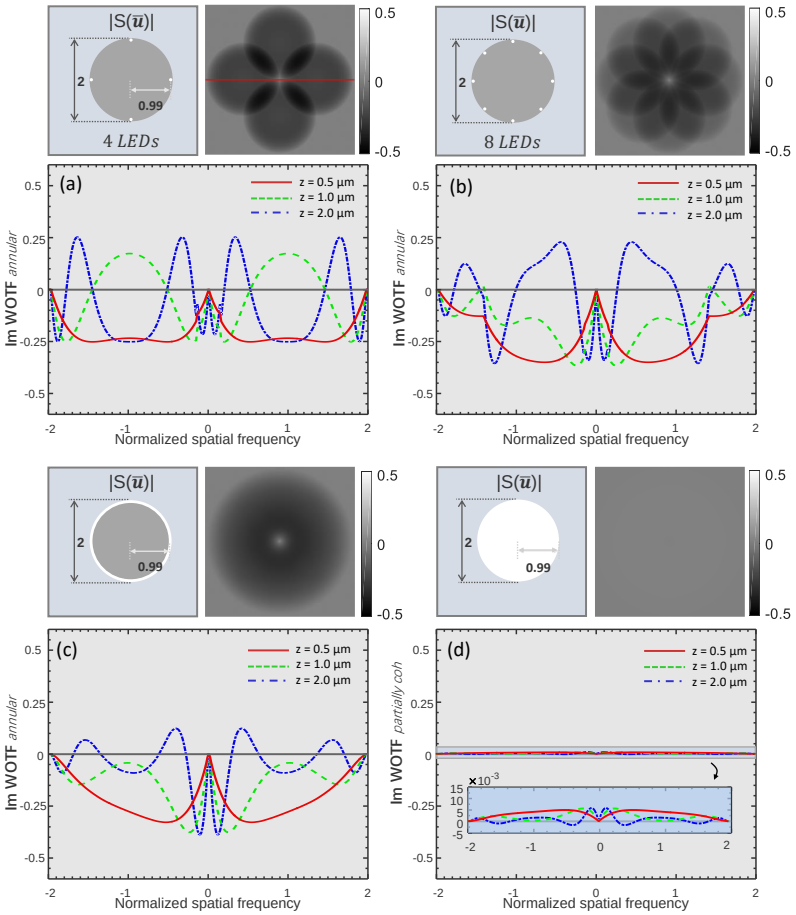

Fig. 2. (a-c) 2D images of PTF and line profiles of three different types discrete annular illumination patterns for various defocus distances. (d) Traditional circular diaphragm aperture and corresponding PTF.

corresponding to the phenomenon that the larger aperture diaphragm provides higher imaging resolution but the phase contrast of defocused image is too weak to capture. The aperture of circular illumination must be stopped down to produce appreciable contrast for phase information, but it is not necessary for the annular illumination. Here, it is worth noting that the number of LEDs located on the edge of source pupil N should be as much as possible for isotropic imaging resolution in all directions, but we choose the eight LEDs as the proposed illumination pattern considering the finite spacing between two adjacent LED elements.

From the profiles of PTF for various aperture shapes and defocus distances, all four illumination patterns have twice frequency bandwidth of objective NA, but the PTF response of circular illumination is too weak. The phase information can hardly be transferred into intensity via defocusing when the illumination NA is large, and the weak contrast of defocused intensity image would lead to poor SNR. The number of zero crossings of PTF for large defocus distance is more than the small one due to the rhythmical fluctuation of WOTF imaginary part, and it is difficult to recover the phase from measured intensity around these point. Thereby, the proposed annular LED illumination approach not only extends the imaging resolution to twice the NA of the objective in most directions, but also provides the robust response of phase contrast for captured intensity stack.

Biomedical Optics EXPRESS

2.3. QPI via TIE and WOTF inversion

In the paraxial regime, the wave propagation is mathematically described by the Fresnel diffraction integral [25], while the relationship between the intensity and phase during wave propagation can be described by TIE [15]:

$$-k\frac{\partial I(\boldsymbol{r})}{\partial z} = \nabla_\perp \cdot [I(\boldsymbol{r})\nabla_\perp \phi(\boldsymbol{r})] \tag{15}$$

where k is the wave number $2\pi/\lambda$, $I(\boldsymbol{r})$ is the intensity image in the in-focus plane, $\nabla_\perp$ denotes the gradient operator over the transverse direction $\boldsymbol{r}$, $\cdot$ denotes the dot product, and $\phi(\boldsymbol{r})$ represents the phase of object. The left hand of TIE is the spatial derivative of intensity in the in-focus plane along z axis. The longitudinal intensity derivative $\partial I/\partial z$ can be estimated through the difference formula $(I_1 - I_2)/2\Delta z$, where I_1 and I_2 are the two captured defocused intensity images, and Δz is the defoucs distance of axially displaced image. By introducing the Teague's auxiliary function $\nabla_\perp \psi(\boldsymbol{r}) = I(\boldsymbol{r})\nabla_\perp \phi(\boldsymbol{r})$, the TIE can be converted into the following two Poisson equations:

$$-k\frac{\partial I(\boldsymbol{r})}{\partial z} = {\nabla_\perp}^2 \psi \tag{16}$$

and

$$\nabla_\perp \cdot (I^{-1}\nabla_\perp \psi) = {\nabla_\perp}^2 \phi \tag{17}$$

The solution for ψ can be obtained by solving the first Poisson equation Eq. (16), thus the phase gradient can be obtained as well. The second Poisson equation Eq. (17) is used for phase integration, and the quantitative phase $\phi(\boldsymbol{r})$ can be uniquely determined by these two Poisson equations. For a special case of pure phase object (eg. unstained cells and tissues), the intensity image on the in-focus plane can be treated as a constant because the untainted cells is almost transparent. Thus, the TIE can be simplified as only one Poisson equation:

$$-k\frac{\partial I(\mathbf{r})}{\partial z} = I(\mathbf{r})\nabla^2 \phi(\mathbf{r}) \tag{18}$$

Then, the fast Fourier transform (FFT) solver [18–20] is applied to Eq. (18), and the forward form of TIE in the Fourier domain corresponds to a Laplacian filter

$$\frac{\widetilde{I_1}(\mathbf{u}) - \widetilde{I_2}(\mathbf{u})}{4\widetilde{I}(\mathbf{u})} = \left(\pi\lambda z|\mathbf{u}|^2\right)\widetilde{\phi}(\mathbf{u}) \tag{19}$$

The inverse Laplacian operator $1/(\pi\lambda z|\mathbf{u}|^2)$ is analogous to an inversion of CTF or weak defocusing PTF in the coherent limit.

For partially coherent illumination, the traditional form of TIE is not suitable for the phase retrieval since this equation contains no parameters about imaging system. In order to take the effect of partial coherence and imaging system into account, the Laplacian operator $\pi\lambda z|\mathbf{u}|^2$ of TIE in the Fourier space should be replaced by the PTF of arbitrary axis-symmetric source. The ATF $H_A(\mathbf{u})$ and PTF $H_P(\mathbf{u})$ are determined by the real and imaginary part of WOTF respectively, as shown in Eq. (7). Thus, the ATF is an even function while the PTF is always an odd function for different defocus distances. On the condition that the defoucs distances of two captured intensity images are same and defocus directions are opposite, the subtraction between two intensity images give no amplitude contrast but a pure double phase contrast. Therefore, the in-focus image $I(\boldsymbol{r})$ is treated as the background intensity and the forward form of WOTF can be expressed as:

$$\frac{\widetilde{I_1}(\mathbf{u}) - \widetilde{I_2}(\mathbf{u})}{4\widetilde{I}(\mathbf{u})} = \mathrm{Im}\left[WOTF(\mathbf{u})\right]\widetilde{\phi}(\mathbf{u}) \tag{20}$$

Biomedical Optics EXPRESS

Equation (20) makes the relationship between phase and PTF linear, then QPI can be realized by the inversion of WOTF in Fourier space

$$\phi(\mathbf{r}) = \mathscr{F}^{-1}\left\{\frac{\widetilde{I}_1(\mathbf{u}) - \widetilde{I}_2(\mathbf{u})}{4\widetilde{I}(\mathbf{u})}\frac{\mathrm{Im}\left[WOTF(\mathbf{u})\right]}{|\mathrm{Im}\left[WOTF(\mathbf{u})\right]|^2 + \alpha}\right\} \tag{21}$$

where $\mathscr{F}^{-1}$ denotes the inverse Fourier transform, and α is the Tikhonov-regularization parameter, which is usually used in the Wiener filter to set maximum amplification, avoiding the division by zero of WOTF.

First, we implement our method to the phase reconstruction of a simulated resolution target. The resolution test image is used as an example phase object defined on a square region and the grid width is 512 pixels with a pixel size of 0.176 μm. The wavelength of illumination is 530 nm, and the objective NA is 0.75. Considering the spatial coherence of LED source, the luminous source size of LED is represented by a cross shape containing five pixels in this square frequency spectrum. The captured defocused intensity images are noise-free and the defocus distance is 0.5

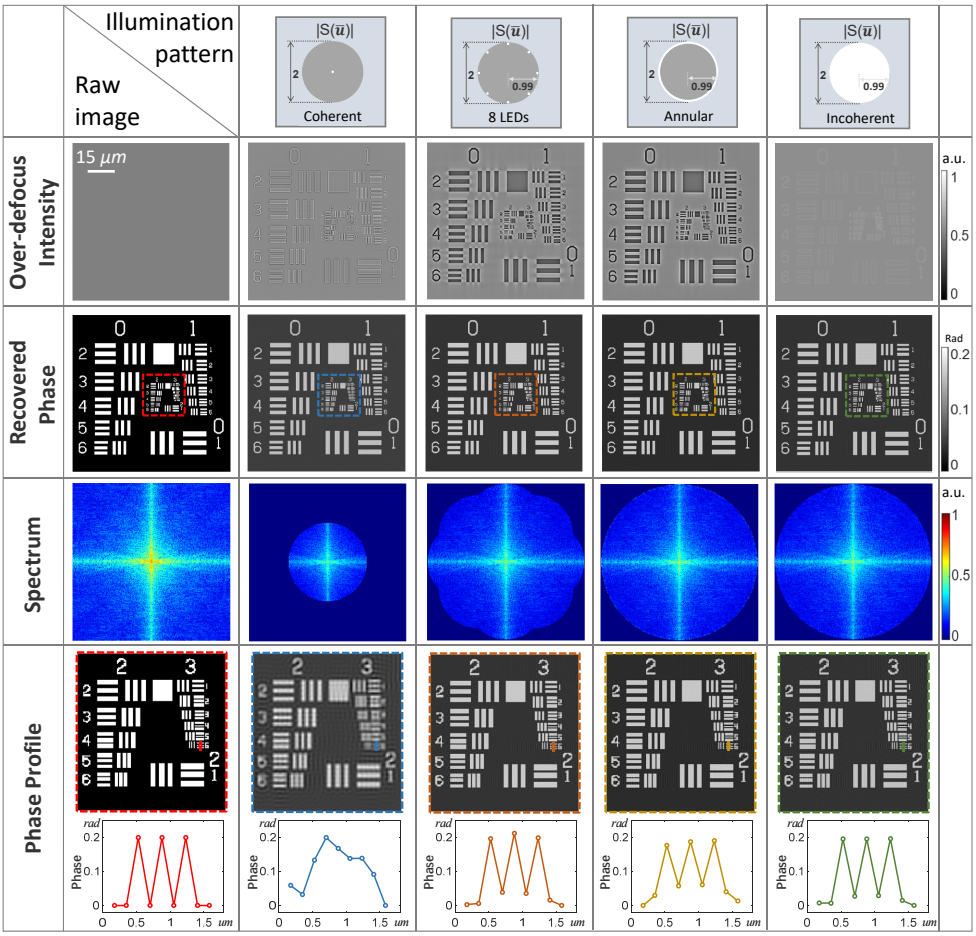

Fig. 3. Various noise-free reconstruction results based on a simulated phase resolution target corresponding different illumination patterns. The parameters of optical system and pixel size of camera is set to satisfy the Nyquist sampling criterion, and the sampling frequency of camera equals twice imaging resolution of objective NA. Scale bar, 15 μm.

Biomedical Optics EXPRESS

μm. The WOTF for various illumination patterns can be derived using Eq. (9) and Eq. (11), and the inversion of WOTF is applied to the Fourier transform of captured intensity stack. The detailed reconstruction results of resolution target under different illumination patterns are shown in Fig. 3. The maximum sampling frequency of camera is set to the same as twice imaging resolution of objective NA. The center region of simulated resolution target is enlarged and marked with the dashed rectangle. As predicted by the WOTF of corresponding illumination pattern, the recovered Fourier spectrum is determined by the cutoff frequency of WOTF. Moreover, the measured phase profiles of the smallest resolution elements in the group 3 of this simulated target are plotted in the last row of sub-figure. It can be seen that the edge of the reconstructed resolution elements under coherent illumination is distorted and blurry, but the smallest elements in the group 3 for other three illumination patterns are clear and distinguishable. Even though the imaging resolution is improved by using annular or nearly incoherent illumination, it is almost impossible to recover the full Fourier spectrum of object phase. The Gibbs ringing artifacts of individual resolution elements are superimposed on each other, and the background of recovered phase profile is not coming flat due to the truncation of original Fourier spectrum by imaging system.

In order to characterize the noise sensitivity of proposed approach, another simulated result is presented in Fig. 4 as well. The system parameters used in this simulation are the same as above one, but each defocused intensity image is corrupted by Gaussian noise with standard deviation of 0.1 to simulate the noise effect. The Fourier spectrum of test object is reconstructed

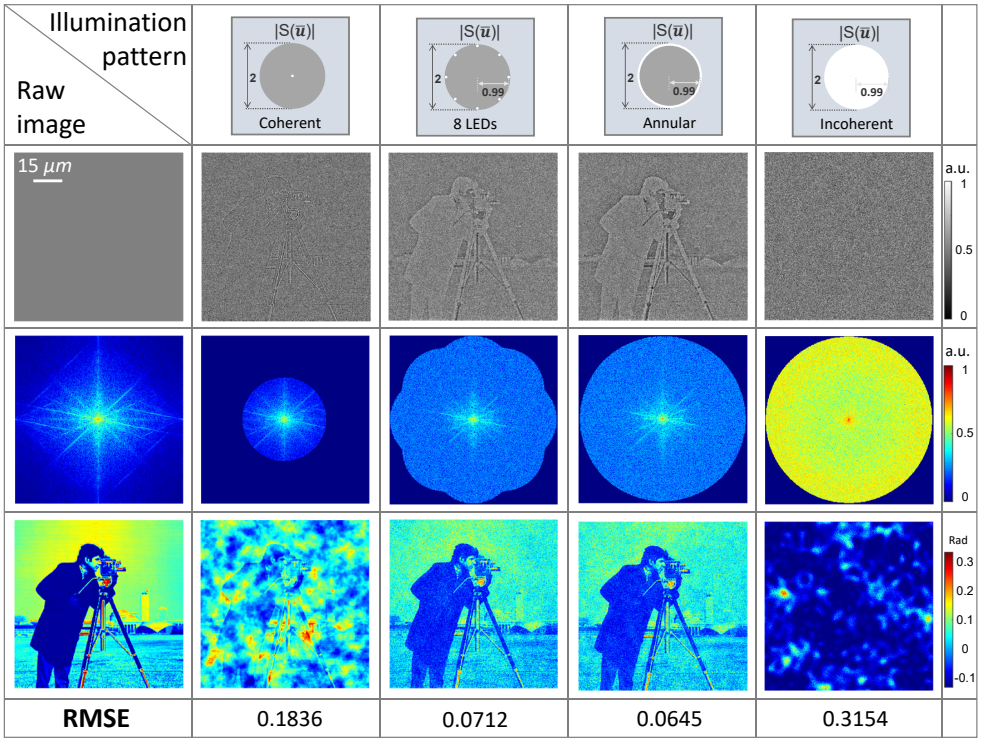

Fig. 4. Phase reconstruction results under the Gaussian noise with standard deviation of 0.1. The response of transfer function rises slowly at low frequencies leading the over-amplification of noise, and there are cloud-like artifacts superimposed on the reconstructed phases for coherent illumination. While the values of WOTF of traditional circular aperture is too close to zero and leads to the over-amplification of noise at both low and high frequency. Scale bar, 15 μm.

Biomedical Optics EXPRESS

by the inversion of WOTF, and the final retrieved phase is evaluated by the root-mean-square error (RMSE). From this diagram, the cutoff frequency of PTF using coherent illumination is still restricted to coherent diffraction limit, but the other three illumination patterns can extend the cutoff frequency to twice the NA of the objective. The recovered phase of coherent illumination aperture is contaminated by the cloud-like noise and the incoherent one is submerged in both low frequency and high frequency noise. In contrast, the low frequency noise is greatly reduced in the retrieved phase images using the annular illumination patterns, and most of high frequency components are recovered except for the decreased background.

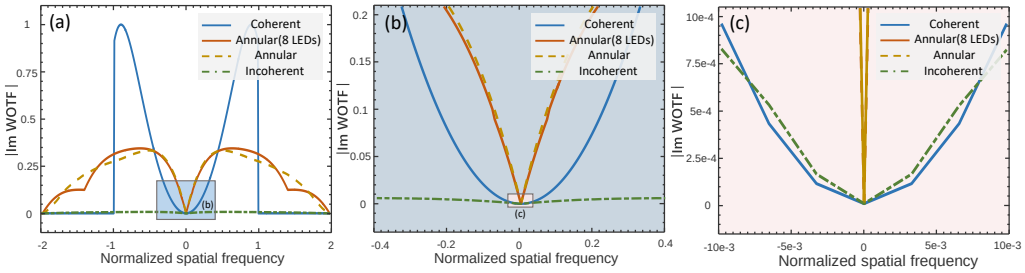

Fig. 5. (a) Magnitudes of PTF profiles for four different types different illumination patterns under weak defocusing. (b) Enlarged profiles of blue-boxed regions. The response of annular apertures rises faster than other two illumination patterns. (c) Further enlarged profiles of red-boxed regions. The magnitude of incoherent PTF is slightly larger than the coherent one near zero frequency.

Although the coherent illumination can provide bigger magnitude of PTF (unit 1 approximatively), as shown in Fig. 5(a), the slow rising of PTF at low frequency leads to the superimposition of cloud-like artifacts on the reconstructed phase or the decrease of background for noise-free case. The value of WOTF of incoherent circular aperture is too close to zero and this poor response would result the over-amplification of noise at both low and high frequency. Therefore, the proposed annular illumination method provides not only the twice resolution of objective NA but also the robust response of transfer function. And the accuracy and stable quantitatively retrieved phase of the test object is given finally.

3. Experimental setup

As depicted in Fig. 6(a), the experimental setup is composed of three major components: a programmable LED array, a microscopic imaging system, and a CMOS camera. The commercial surface-mounted LED array is placed in the front focal plane of the condenser as illumination source, and each LED can provide approximately spatially coherent quasi-monochromatic illuminations with narrow bandwidth (central wavelength λ = 530 nm, ~ 20 nm bandwidth). Thus, the light emitted from the condenser lens for single LED can be nearly treated as a plane wave. The distance between every adjacent LED elements is 1.67 mm, and only a fraction of whole array is used for programmable illumination because the original resolution of this commercial LED array is 64 × 64 and the diameter of circular condenser aperture is only about 35 mm. The array is driven dynamically using a LED controller board, which is custom-built by ourselves with a Field Programmable Gate Array (FPGA) unit, to provide the various illumination patterns, and the camera is synchronized with the hardware board for each intensity frame.

In our work, the discrete annular LED illumination pattern matched with objective pupil is displayed on the array, as shown in Fig. 6(b). Figure 6(c) is taken in the objective back focal plane by inserting a Bertrand lens into one of the eyepiece observation tubes or removing the eyepiece tubes. The microscope is equipped with a scientific CMOS (sCMOS) camera (PCO.edge 5.5,

Biomedical Optics EXPRESS

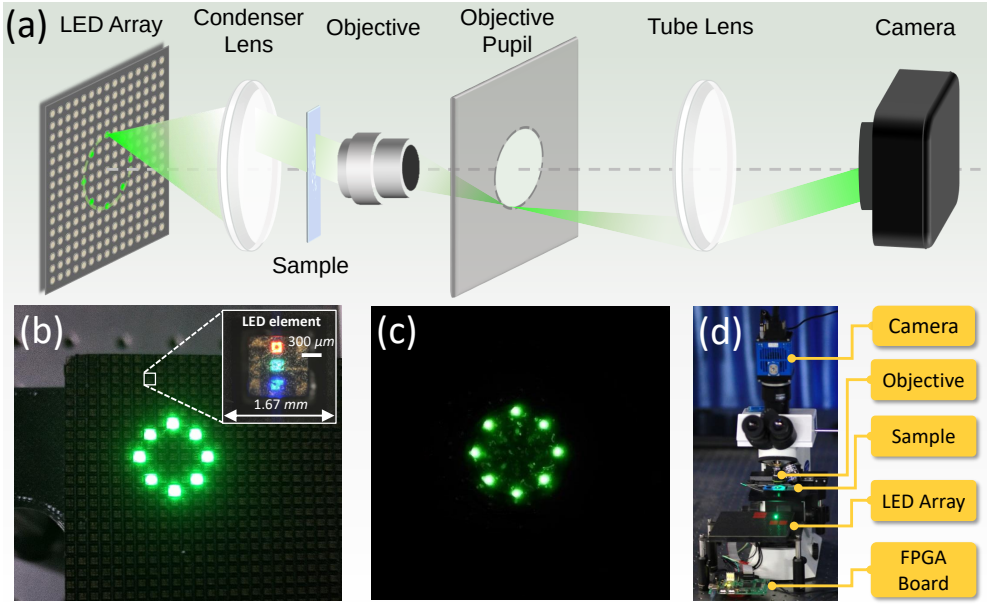

Fig. 6. (a) Schematic diagram of experimental setup. (b-c) The annular pattern is displayed on the LED array and the size of this annulus is matched with objective pupil in the back focal plane. (d) Photograph of whole imaging system. The LED array is placed beneath the sample and the crucial parts of setup in this photo are marked with the yellow boxes. Scale bar represents 300 μm.

6.5 μm pixel pitch) and a universal plan objective (Olympus, UPlan 20 ×, NA = 0.4). Another universal plan super-apochromat objective (Olympus, UPlan SAPO 20×, NA = 0.75) and a higher sampling rate detector (2.2 μm pixel pitch) are also utilized for higher resolution imaging result. The total time of intensity image stack acquisition is about 3 seconds and the data is processed by MATLAB software. Moreover, we implement the 2D FFT on a graphics processing unit (GPU, NVIDIA GeForce GTX970M), and the time required for all computation processes of square field of view (FOV) (2160 × 2160) is about 2.5 seconds. The photograph of whole imaging system is illustrated in Fig. 6(d) and the crucial parts of setup in this photo are marked with the yellow boxes. A short video of switching process between two different objective lenses based on programmable LED illumination is shown in Visualization 1.

4. Results

4.1. Quantitative characterization of control samples

In order to validate the accuracy of proposed QPI approach based on annular LED illumination, the micro polystyrene bead (Polysciences, n=1.59) with 8 μm diameter immersed in oil (Cargille, n=1.58) is measured using 0.4 NA objective and sCMOS camera. The sample is slightly defocused, and three intensity images are recorded at ± 1 μm planes and in-focus plane. By invoking the inversion of WOTF, the reconstructed quantitative phase image of beads, which is a sub-region of whole FOV, is shown in Fig. 7(a1). The horizontal profile through the center of a single bead is illustrated as the solid brown line in Fig. 7(a2), and the blue dash line represents the theoretically quantitative phase of the micro polystyrene bead. Of interest in these results is excellent agreement between the magnitude and shape of the compared bead profile. There is still some slightly high frequency noise in the retrieved phase image due to the amplification of noise near the cutoff frequency, but these artifacts do not affect the accuracy and feasibility of

Biomedical Optics EXPRESS

our proposed method.

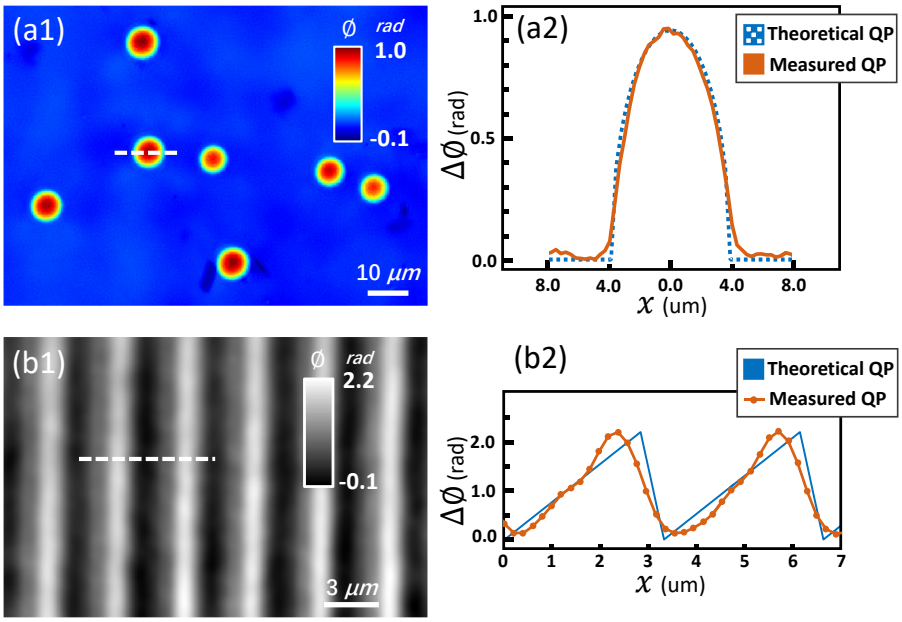

Fig. 7. (a1-b1) Reconstructed phase distributions of the micro polystyrene bead with 8 μm diameter and blazed transmission grating with 3.33 μm period. (a2-b2) Measured quantitative phase line profiles for a single bead and a few periods grating. Theoretical (90^o groove angles for grating) line profiles are also plotted for reference. Scale bar denotes 10 μm and 3 μm, respectively.

Furthermore, a visible blazed transmission grating ($Thorlabs\ GT13-03$, grating period Λ = 3.33 μm, blaze angle θ_B = 17.5^o) is employed in the quantitative experiment using the same method and procedures. The grating is made by Schott B270 glass (n_{glass} = 1.525), and mounted face up on a glass slide with refractive index matching water (n_{water} = 1.33) and a thin *no*. 0 coverslip. Considering that the large pixel size of sCMOS camera and high density of grating, a higher NA objective (NA = 0.75) and sampling rate detector (2.2 μm pixel size) are utilized for the measurement of this grating. Figure 7(b1) represents measured phase image of a sub-region grating for a 23.7 μm × 15.6 μm rectangular patch. Plotted for reference is the theoretical profiles in blue solid line, assuming 90^o groove angles, and also plotted in Fig. 7(b1) is a few periods of the associated brown dot-solid line profiles with no interpolation. These two curves are well consistent with each other excepting the falling edges of phase profile owing to the rapid change of falling edge of grating, and some high frequency components of the sharp edge of this periodic grating can not be recovered. Even so, the two groups quantitative characterizations of control samples further indicate success and accuracy of our method basically.

4.2. *Experimental results of biological specimens*

As demonstrated by the previous simulation results in subsection 2.3, the developed approach of annular LED illumination can provide twice imaging resolution of objective NA and noise-robust response of transfer function. We also test the proposed reconstruction method in its intended biomedical observation experimentally, and the unstained lung cancer cell (LC-06) is used for QPI firstly with 0.4 NA objective and 6.5 μm pixel pitch camera. Figure 8(a1) and 8(a2) are the quantitative phase images of LC-06 defined on a square FOV for point source and annular source, respectively. The point source is the central LED of the used region of whole array, and this

Biomedical Optics EXPRESS

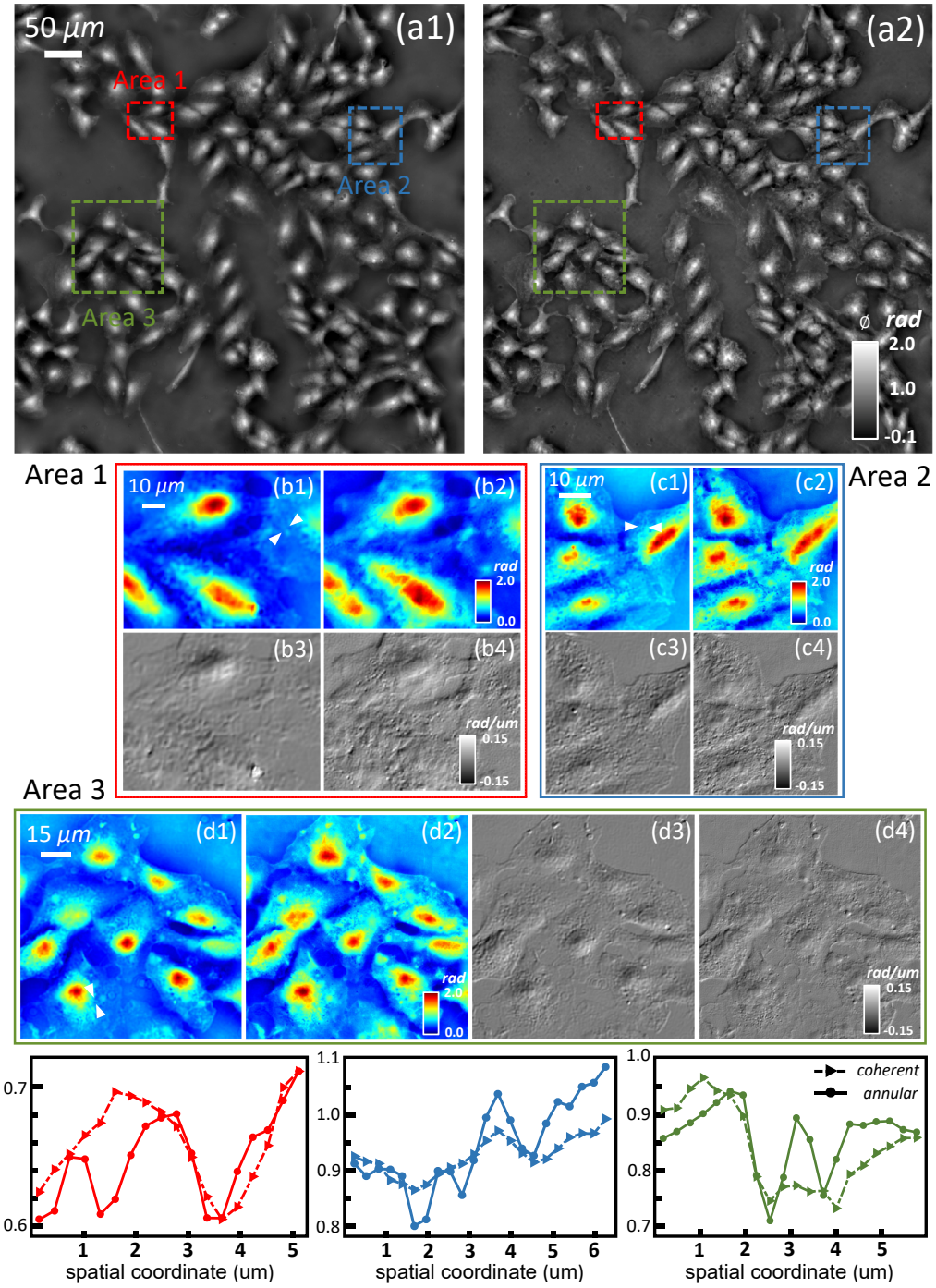

Fig. 8. (a) Quantitative reconstruction results of LC-06 with 0.4 NA objective and 6.5 μm pixel pitch camera for coherent and discrete annular illumination. (b-c) Three enlarged sub-regions of quantitative maps and simplified DIC images are illustrated as well. The white arrows shows line profiles taken at different positions in the cells. Scale bar equals 50μm, 10μm and 15μm, respectively.

Biomedical Optics EXPRESS

coherent source coincides with the system optical axis. Three representative sub-areas of whole quantitative map are selected and enlarged for more detailed descriptions. The phase images of three enlarged sub-regions are shown in jet map, and the correspondingly simplified DIC images are illustrated in Fig. 8(b) and 8(c).

From these quantitative phase and phase gradient images, it is obvious that the phase imaging resolution of annular illumination source is higher than the coherent one. Some tiny grains in cytoplasm are sharper and more vivid, and it is important to indicate the stages of cell during the whole cell cycle. In addition, the white arrows show line profiles taken from two different positions in the cells, and the comparative phase profiles are presented in different color lines in Fig. 8. These plot lines demonstrate that the significant improvement of high frequency features using annular aperture compared to the coherent illumination. Thus, the allowed highest spatial frequency of QPI base on annular LED illumination is 0.8 effective NA (0.66μm) in phase reconstruction as predicted by the the cutoff frequency of PTF.

Then, our system is used for the QPI of label-free HeLa cell by replacing the objective and the camera with another 0.75 NA objective and 2.2 μm pixel size camera. The FOV is 285.1 $\times$ 213.8 μm^2 with the sampling rate of 0.11 μm in the object plane. Figure 9(a) and 9(b) show the images of high resolution quantitative phase and the phase gradient in the direction of the image shear (45^o). As can be seen in Fig. 9(c)–9(e), three sub-regions are selected by solid rectangular shape for no resolution loss of phase images. The last column of Fig. 9 are the enlarged quantitative phase images of corresponding sub-regions under coherent illumination.

For this group of quantitative results, we will not repeat the resolution improvement of annular LED illumination but point out some defects in the phase images. The background of this quantitative phase image in Fig. 9(a) is not "black" enough, and the reason for the decrease of background contrast is the loss of low frequency components of Fourier spectrum. The response of PTF near zero point determines the low frequency SNR of retrieved phase image, as shown

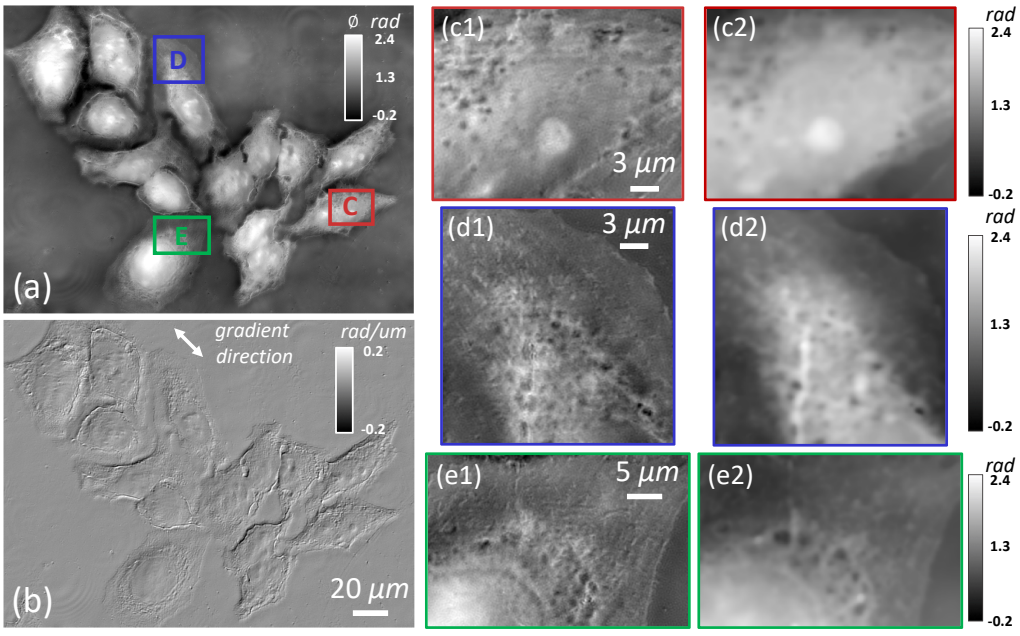

Fig. 9. (a) High resolution QPI of HeLa cell with 0.75 NA objective. (b) Simulated DIC image. (c-e) Three enlarged sub-regions of quantitative phase of HeLa cell under coherent and discrete annular source. Scale bar equals 20μm, 3μm and 5μm, respectively.

Biomedical Optics EXPRESS

in Fig. 5. Although the PTF response of annular illumination is robust among these presented patterns, it is still difficult to recovered the completely low frequency spectrum of measured object.

5. Discussion and conclusion

In summary, we demonstrate an effective QPI approach based on programmable annular LED illumination for double imaging resolution of objective NA and noise-robust reconstruction of quantitative phase. The WOTF of axis-symmetric oblique source is derived using the concept of TCC, and the WOTF of discrete annular aperture is validated with the incoherent superposition of the individual point sources. The inversion of WOTF is applied to the intensity stack containing three intensity images with equal and opposite defoci, then the quantitative phase can be retrieved. The recovered phase of simulated resolution target and noise-corrupted test image prove that the proposed illumination pattern can extend imaging resolution to twice NA of objective and give great noise insensitivity. Furthermore, the biological samples of human cancer cell are imaged with two different types objective, and the imaging resolution of retrieved phase is enhanced compared to the coherent illumination indeed. Besides, this QPI setup is easily fitted into a conventional optical microscope after small modifications and the programable source makes the modulation of annular pattern more flexible and compatible without customized-build annuli matched objective pupil.

However, there are still some important issues that require further investigation or improvement in this work. The experiment based on a real phase resolution target is lacking, and a factor of imaging resolution improvement of proposed method relative to coherent illumination has not been given in the results yet. And the response of proposed transfer function is not robust enough to recover the completely low frequency spectrum of measured object, which would decrease background contrast of retrieved phase image. Another shortcoming of this modified microscopic imaging system is that it is difficult to apply the long-term time-elapse living cellular imaging to these relatively low end bright-field microscope, like Olympus CX22 microscope, different from our early work based on IX83 microscope. To solve this problems, a special sample cuvette is required for the imaging of living biological cells and the additional devices may be needed to modify our setup, such as a smaller spacing and brighter LED array. Despite these existing drawbacks, the configuration of this system takes full advantage of the compatibility and flexibility of the programmable LED illumination and bright-field microcopy. And the annular illumination pattern gives the quantitative demonstration of control samples and promising results of biological specimens.

Appendix

A. Derivation of intensity formation under partially coherent illumination using Hopkins' formulae

In the main text, the standard optical microscope system can be simplified as an extended light source, a condenser lens, a sample, an objective lens, and a camera on the image plane. Based on Abbe's theory [47], the captured image of object at the image plane can be interpreted as the summation of all the source points of the illumination. For each source point, the optical formation is described by Fourier-transforms and a linear filtering operation as a linear system, and the electrical field $E(x, y)$ on the camera plane can be expressed as

$$E(x, y; f_c, g_c) = \iint t(f, g)\, h(f + f_c, g + g_c) \exp\left[-i2\pi (fx + gy)\right] df\, dg \tag{22}$$

Where t is the complex transmittance of object, and h represents the amplitude PSF of the imaging system. The intensity on the image plane is proportional to the square magnitude of the

Biomedical Optics EXPRESS

electric field distribution and takes the form of

$$\begin{aligned} I(x,y) &= S(f_c,g_c)\,|E(x,y;f_c,g_c)|^2 df_c dg_c \\ &= S(f_c,g_c)\,|\mathscr{F}[t(f,g)\,h(f+f_c,g+g_c)]|^2 df_c dg_c \end{aligned} \tag{23}$$

Where $I(x, y)$ is the intensity of the object captured at the image plane, $S(f_c, g_c)$ is the distribution of extended light source, and $\mathscr{F}$ denotes Fourier transform. By interchanging the order of integration, we can express Eq. (23) according to Hopkins' formulation [48, 49]

$$\begin{aligned} I(x,y) = \iiiint & S(f_c,g_c)\,P\left(f'+f_c,g'+g_c\right)P^*\left(f''+f_c,g''+g_c\right)T\left(f',g'\right)T^*\left(f'',g''\right) \\ & \exp\left[-i2\pi\left(f'-f''\right)x - i2\pi\left(g'-g''\right)y\right] df'\,dg'\,df''\,dg'' \end{aligned} \tag{24}$$

Where P is the coherent transfer function with the objective pupil function $|P|$, and T is the spatial object spectrum respective to the Fourier transform of object complex transmittance t. Here, we separate the contributions of the specimen and system, and the transmission cross coefficient (TCC) is introduced as a combination of the source and pupil expressed as

$$TCC\left(f',g';f'',g''\right) = \iint S(f_c,g_c)\,P\left(f'+f_c,g'+g_c\right)P^*\left(f''+f_c,g''+g_c\right)df_c dg_c \tag{25}$$

By replacing the variable $\left(f',g'\right)$ and $\left(f'',g''\right)$ with two 2D vector $\mathbf{u}_1$ and $\mathbf{u}_2$ in frequency domain, and the Eq. (25) can be simplified as

$$TCC(\mathbf{u}_1;\mathbf{u}_2) = \iint S(\mathbf{u})\,P(\mathbf{u}+\mathbf{u}_1)\,P^*(\mathbf{u}+\mathbf{u}_2)\,d\mathbf{u} \tag{26}$$

Then, the final intensity of object on the image plane can be rewritten in 2D vector variable

$$I(\mathbf{r}) = \iint TCC(\mathbf{u}_1;\mathbf{u}_2)\,T(\mathbf{u}_1)\,T^*(\mathbf{u}_2)\exp\left[i2\pi\mathbf{r}(\mathbf{u}_1-\mathbf{u}_2)\right]d\mathbf{u}_1 d\mathbf{u}_2 \tag{27}$$

Funding

This work was supported by the National Natural Science Fund of China (61722506, 61505081, 111574152), Final Assembly '13th Five-Year Plan' Advanced Research Project of China (30102070102), National Defense Science and Technology Foundation of China (0106173), Outstanding Youth Foundation of Jiangsu Province of China (BK20170034), 'Six Talent Peaks' project of Jiangsu Province, China (2015-DZXX-009), '333 Engineering' Research Project of Jiangsu Province, China (BRA2016407), Fundamental Research Funds for the Central Universities (30917011204, 30916011322), Open Research Fund of Jiangsu Key Laboratory of Spectral Imaging & Intelligent Sense (3091601410414).

Disclosures

The authors declare that they have no conflicts of interest related to this article.